Korean J. Chem. Eng., 33(6), 1788-1798 (2016)
DOI: 10.1007/s11814-016-0051-4

pISSN: 0256-1115
eISSN: 1975-7220

Facile synthesis of $TiO_2/ZnFe_2O_4$ nanocomposite by sol-gel auto combustion method for superior visible light photocatalytic efficiency

Kalithasan Natarajan[*,**], **Puspendra Singh**[*], **Hari Chand Bajaj**[*,**], **and Rajesh Jagannath Tayade**[*,†]

*Inorganic Materials and Catalysis Division (IMCD), CSIR-Central Salt and Marine Chemicals Research Institute (CSIR-CSMCRI),
Council of Scientific and Industrial Research (CSIR), G. B. Marg, Bhavnagar-364 002, Gujarat, India
**Academy of Scientific and Innovative Research (AcSIR), CSIR-Central Salt and Marine Chemicals Research Institute (CSIR-CSMCRI),
G. B. Marg, Bhavnagar-364 002, Gujarat, India

(*Received 19 October 2015 • accepted 18 February 2016*)

Abstract−Photocatalytic composite materials having photon absorption capability in the range of visible light were synthesized by loading TiO_2 (5, 10, 15, and 20 wt%) on ferrite nanocomposites by sol-gel auto-combustion method. The synthesized nanocomposites were analyzed using X-ray diffraction, Transmission electron microscopy, diffuse reflectance spectroscopy and N_2 adsorption techniques. The generation of photo active hydroxyl radicals for all the synthesized composites was found higher under the irradiation of red LED (RLED irradiation) which was confirmed by degradation of rhodamine B dye under irradiation of RLED. Photocatalytic activity of the synthesized nanocomposites was also carried out under irradiation of ultraviolet (UVLED) and blue (BLED) light emitting diodes, which is comparatively less than for the reaction under red LED irradiation. The operational parameters like catalyst amount, pH and concentration of dye solution were studied and ESI-MS degradation pathway is proposed by analyzing the degraded samples.

Keywords: TiO_2 Loading, Zinc Ferrite, Light Emitting Diodes (LEDs), Rhodamine B, Photocatalysis

INTRODUCTION

The utilization of photocatalytic processes for environmental cleanup has not yet reached up to the mark due to the non-commercialization of this process. Many efforts have been made to enhance the photocatalytic activity for the degradation of pollutant present in air and water under ultraviolet light irradiation [1-4]. The sources for these ultraviolet lights were natural solar light, which contains 5-8% ultraviolet light, and another is conventional high/medium/low pressure mercury vapor lamp [5-8]. The use of mercury based conventional ultraviolet lamps provides efficient photocatalytic degradation, but they consume higher energy, owns hazardous mercury and also need cooling while in operation. From the literature, it is also evident that the use of solar light is not effective to carry out the photocatalytic degradation of pollutant effectively and also needs higher space [9-12]. Recently, light emitting diodes have been used as alternative sources which do not contain mercury, consume low energy, robust, smallhess, cheaper and can be utilized with freedom to design various geometry of reactor designing [13-16].

Till today, particularly ultraviolet LEDs have been used for the application of environmental cleanup. However due to economic concerns, few efforts also made to utilize visible LEDs for the photocatalytic degradation of environmental pollutants, which can lead to providing an energy efficient, economic and feasible process. The utilization of the visible LEDs could be possible based on the photocatalytic efficiency of the synthesized photocatalysts [17-20]. The efficiency of the photocatalytic materials can be tuned by increasing surface area, optimizing electron hole pair recombination and by tuning the bandgap. In the past, many materials, such as TiO_2, ZnO and CdS, have been used for the photocatalytic application under irradiation of solar and ultraviolet light irradiation having bandgap in the range of 2.5 to 3.5 eV [21-24].

Zinc ferrite (ZF) based photocatalytic materials have also demonstrated their applicability for the degradation of pollutant in presence of visible light irradiation. These ZF materials have narrow bandgap (1.86 eV), chemical stability and sensitivity to visible light, making them as a promising material for photocatalytic application as well as hydrogen production. Even though, ZF cannot be utilized directly for the photocatalytic degradation of toxic organic compounds due to lower valence band potential [25-29]. This can be overcome by metal doping and coupling with other semiconductor nanomaterials by which the photocatalytic activity could be achieved effectively under UV as well as visible light irradiation. Since TiO_2 has high photo activity under UV light irradiation, it has been coupled with ZF and their photocatalytic activities were studied under visible light irradiation. The methods, namely sol-gel, co-precipitation, colloid chemistry, hydrothermal, solid state reaction and microwave methods, have been utilized for the synthesis of ZF and TiO_2/ZF nanocomposites, which needs considerable time and energy [30-35]. This can be overcome by the fast and reliable auto combustion method; the major advantage about this method is the avoidance of heating the synthesized materials in an oven to remove moisture. Moreover, from the literature it is evident that

---

[†] To whom correspondence should be addressed.

E-mail: tayade@csmcri.org, rtayade@gmail.com

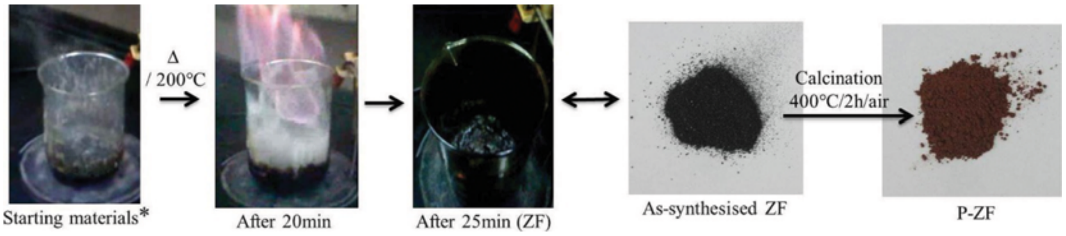

Fig. 1. Schematic representation of the sol-gel auto combustion process for photocatalysts synthesis (*$Zn(NO_3)_3 \cdot 6H_2O$+$Fe(NO_3)_3 \cdot 9H_2O$+dry ethanol+DEA).

the light sources utilized for the degradation reactions in presence of ZF and ZF nanocomposite photocatalysts were mostly high pressure and low pressure mercury vapor lamp, xenon lamp etc. which was being studied by the researchers widely [36-38].

In present study, we have tried to explore the effective utilization of red LEDs (RLEDs) for photocatalytic degradation of rhodamine B (RhB) dye using pristine ZF (P-ZF) and TiO_2/ZF (TZF) nanocomposite photocatalysts. The sol-gel auto combustion method was chosen for the synthesis of zinc ferrite nanocomposite photocatalysts, considering the requirement of low energy consumption, less time, and lower agglomeration of particles during synthesis as compared to processes like solvothermal, hydrothermal, co-precipitation and sol-gel. Additionally, all the catalysts synthesized by reported methods have demonstrated their photocatalytic activity under various irradiation sources [44-48]. However, to the best of our knowledge, this is the first report on the degradation of RhB dye using TiO_2/ZF composite under irradiation of Red LED. The structural, textural, electronic and morphological properties of the synthesized nanocomposites were characterized thoroughly using various sophisticated instruments. The photocatalytic activity of the catalysts was also studied under irradiation of blue and ultraviolet LEDs and compared. In addition, the degradation pathway of RhB dye was proposed based on electrospray ionization mass spectrometry (ESI-MS) analysis.

EXPERIMENTAL

1. Materials

Zinc Nitrate ($Zn(NO_3)_3 \cdot 6H_2O$) was purchased from Sigma Aldrich, Mumbai, and Ferric nitrate ($Fe(NO_3)_3 \cdot 9H_2O$) was purchased from SD Fine Chemicals Pvt Ltd. which was used as starting material. Diethanolamine (DEA), purchased from Sisco Research Laboratories Pvt Ltd., was selected as a fuel. These three chemicals were used as such without any purification. Absolute ethanol was used as a solvent for the synthesis of P-ZF and T-ZF photocatalysts. Standard chemical reagents for chemical oxygen demand (COD) measurements were purchased from E. Merck India Ltd, Mumbai, India. Different wavelength ranges of LEDs, namely ultraviolet LED (UVLED; 390-410 nm), blue LED (BLED; 430-505 nm) and red LED (RLED; 630-660 nm), were purchased from Bivar, inc - CA (United states). Five numbers of LED were mounted on acrylic sheet for irradiation of LED light on the reaction mixture. The intensity of LED mounted on acrylic sheet was determined by lux meter (Yopco) and it was measured by keeping 1 cm distance between LED setup and Lux meter. The intensities of the utilized LED setup were found to be 21, 64 and 542 lux for UVLED, BLED and RLED respectively.

2. Synthesis of Zinc Ferrite (ZF) and TiO_2/Zinc Ferrite (TZF) Nanocomposite Photocatalysts

The synthesis of ZF was carried out as follows: initially, stoichiometric amounts of zinc nitrate and ferric nitrate were taken in a 500 ml beaker followed by the addition of 100 ml absolute ethanol. Then, 16.7 ml of DEA was added as a fuel and the whole reactant mixture was kept at 200 °C on hot plate to get auto combusted (Fig. 1). The ZF product after auto combustion was allowed to cool for half an hour, grounded and calcined at 400 °C for 2 h under air atmosphere with the ramp rate of 2 °C/min. The calcined catalyst was designated as pristine Zinc Ferrite (P-ZF).

Similarly, TiO_2 loaded ferrite nanocomposite photocatalysts with different composition of TiO_2 (5, 10, 15 and 20 wt%) were synthesized by addition of appropriate amount of titanium isopropoxide (TIP) during the synthesis of ZF. The ZF catalysts having amount of 5, 10, 15 and 20 wt% TiO_2 were designated as 5-TZF, 10-TZF, 15-TZF and 20-TZF. For comparison, P-ZF and standard P25 Degussa (20 wt%) catalyst were mechanically ground and used as a reference catalyst, which was named as 20-MTZF.

3. Characterization

The XRD data of the synthesized photocatalysts were obtained using X-ray diffractometer (XPERT-MPD model PW3050) with Cu Kα1 radiation in the 2θ range of 10-80°. The crystallite size of the P-ZF and TZF photocatalysts was calculated from the X-ray diffraction peak broadening of the (311) plane by the following Scherrer's formula (Eq. (1)),

$$D=k\lambda/\beta\text{Cos}\theta \qquad (1)$$

where D is crystallite size, k is the shape factor, λ is the wavelength of X-ray source, β is FWHM of the (311) diffraction peak and θ is the Bragg's angle. The bandgap was determined using diffuse reflectance spectroscopy (UV-Vis-DRS, Shimadzu UV-3101 PC spectrophotometer) equipped with an integrating sphere and $BaSO_4$ as a reference. The morphology of the synthesized catalysts was analyzed using transmission electron microscope (TEM-JEOL JEM-2010 electron microscope). With TEM images, the particle size of the synthesized P-ZF and T-ZF catalysts was also determined using Gatan microscopy software. The surface area, pore volume and pore diameter of the synthesized catalysts were determined by nitrogen adsorption studies at 77 K using a sorptometer (ASAP-2010, Micromeritics).

4. Photocatalytic Activity

The photocatalytic reactions were carried out using the photocatalytic reactor setup reported earlier by our group [13]. Briefly 25 mg of the synthesized photocatalyst (P-ZF) and 25 ml of aqueous RhB dye solution (1×10^{-5} M) was taken in a 150 ml beaker. The contents were sonicated (2 min) for uniform dispersion of catalyst in dye solution and kept under stirring for about half an hour to reach the adsorption desorption equilibrium. The photocatalytic experiments were conducted under irradiation of RLED (5 no's) for 4 h. During photocatalytic experiment, 1.5 ml of reaction mixture was sampled out after every one hour and centrifuged to separate the photocatalyst. Then the supernatant solution was analyzed by UV-Vis spectrophotometer at a wavelength of 554 nm (the maximum absorption wavelength of RhB dye). The photocatalytic activity of the synthesized 5-TZF, 10-TZF, 15-TZF and 20-TZF was also studied using the same procedure each under RLED, UVLED and BLED irradiation. The degradation of RhB dye was confirmed by COD analysis, measured using a SPECTROQUANT NOVA 60 Photometer and TOC was also analyzed using Elementar, Liqui TOC analyser. ESI-MS experiments were performed to predict the degradation pathway of RhB dye samples using Water Q-TOF micro Y A-260 (Micromass) tandem quadruple orthogonal TOF instrument. The analysis of hydroxyl radical formation was performed using terephthalic acid (TPA) as a probe molecule by Fluorolog Spectrophotometer (Horiba Jobinyvon).

RESULTS AND DISCUSSION

1. Powder X-ray Diffraction Analysis

The PXRD pattern of the synthesized P-ZF and TZF photocatalysts is shown in Fig. 2(a). The existence of main peaks is at 2θ of 30.2, 35.5, 43.1, 53.4, 56.9 and 62.4°, which aspect to the (220), (311), (400), (422), (511) and (440) planes of P-ZF. This confirms the formation of P-ZF without any impurity phase, which is similar to the earlier reported literature [49,50]. Fig. 2(b) shows enlarged peak (311) of the synthesized P-ZF, TZF and 20-MTZF catalysts in which a slight peak shift was observed due to the presence of TiO_2. This is similar to the reported one for the inclusion of metal ion to P-ZF, and this might be due to the confinement of TiO_2 nanoparticles within P-ZF pore channels [51]. The XRD pattern of 20-MTZF composite photocatalyst (Fig. 2(a)) shows less intensity peak for TiO_2 at 2θ around 25.3°. Whereas, the XRD patterns of the synthesized P-ZF and TZF are not showing any peaks corresponding to TiO_2. This may be due to the insertion of TiO_2 inside the crystal lattice of the ZF for TZF photocatalysts. It is observed in Fig. 2(b) that the peak at 2θ=35.5 (311) gets broadened as the content of TiO_2 increases and weak diffraction peaks were observed for 5, 10, 15 and 20-TZF. This is due to the reduction in scattering contrast between pore walls and pores after the pore filling by TiO_2 in the host P-ZF catalyst; thus a decrease in the peak intensity was observed [52].

Table 1. Crystallite size, bandgap, surface area (S_{BET}), pore diameter (D_{pore}) and pore volume (V_{total}) of synthesized P-ZF and TZF photocatalysts

Catalysts	Crystallite size (nm)	Band gap (eV)	S_{BET} (m^2/g)	D_{pore} (nm)	V_{total} (cm^3/g)
P-ZF	36.2	1.99	22.72	16.4	0.12
5-TZF	19.89	1.98	89.07	4.23	0.12
10-TZF	18.71	1.96	110.45	3.9	0.12
15-TZF	13.2	1.96	120.21	4.15	0.13
20-TZF	22.73	1.95	174.05	3.32	0.14
20-MTZF	37.53	2.0	31.49	23.48	0.21

This suggests that the crystallite size would decrease with the increase of TiO_2 in the composite photocatalyst. As expected, a decrease in crystallite size of TZF photocatalysts was also observed (Table 1) up to loading of 15 wt% TiO_2 and then increased at 20 wt% loading of TiO_2 in ZF. This indicates that the pores of ZF are capable to host the TiO_2 up to 15 wt% only. If the weight percentage of TiO_2 exceeds 15 wt%, some amount of TiO_2 does not get inserted in the pores of ZF, which results increase in the crystallite size for 20-TZF. The TiO_2 insertion over the host ZF might be visually evidenced (Fig. 2(b)) with the decrease in peak intensity and this is attributed to two major aspects.

First, the increase in electron density of sorbate molecules (TiO_2) leads to the decrease in residual peak intensity (311) plane of TZFs. Secondly, the loss of sample integrity descends the peaks intensity, which is ultimately due to the ascending percentage of TiO_2 insertion [53]. To get the desired percentages (5, 10, 15 and 20 wt%) of

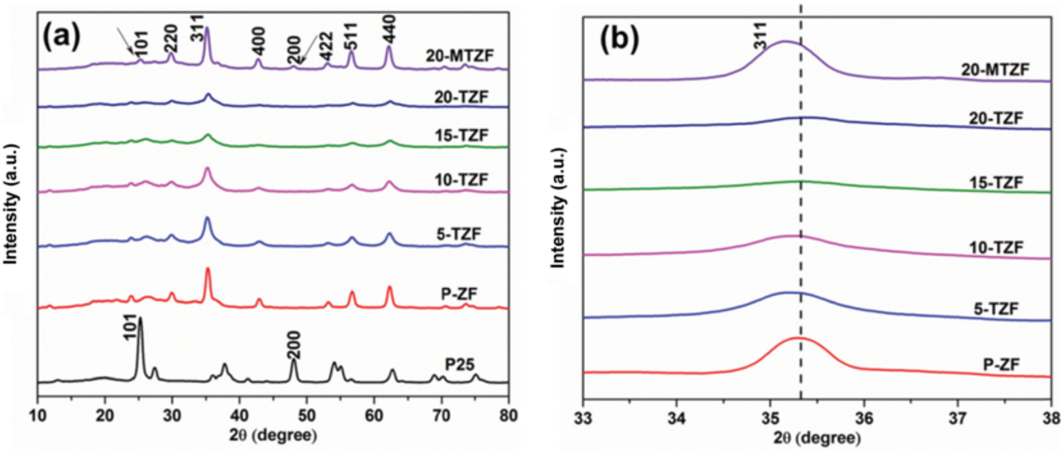

Fig. 2. (a) XRD pattern and (b) enlarged peak of (311) plane of the P-ZF, TZF and MTZF photocatalysts.

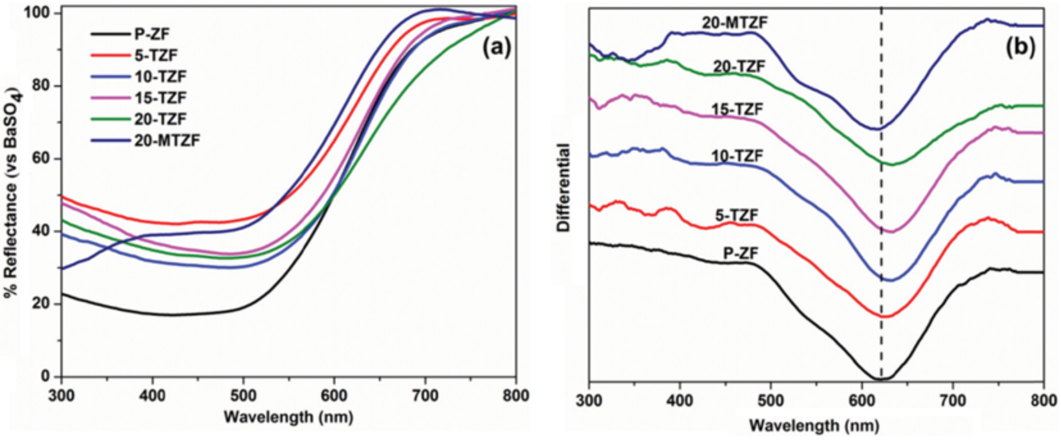

Fig. 3. UV-vis DRS spectrum (a). Differential spectra of the synthesized P-ZF, TZF and 20-MTZF photocatalysts (b).

TiO_2 for synthesizing TZF nanocomposites, the addition of TIP has been varied. Eventually, with the different weight percentages of TiO_2 over ZF, there is a divergence in crystallite size (Table 1), a decrease in major peak (311) intensity as well as peak broadening (Fig. 2(b)). The results in concern about the PXRD studies of our synthesized P-ZF and TZF catalysts were compatible with the reported work about the same type catalysts synthesized using conventional solid state reaction, chemical method, one-step chemical coprecipitation method and a facile calcination process [42,54,78,79].

2. UV-visible Diffuse Reflectance Spectroscopy Analysis

Fig. 3(a) shows the UV-visible diffuse reflectance spectra (UV-vis DRS) of the synthesized P-ZF and TZF catalysts. The reflectance in the visible range of 600-650 nm for the case of P-ZF catalyst is attributed to the electron transition by photoexcitation from O 2p level into Fe 3d level. As the amount of TiO_2 increases for the other four TZF catalysts, the reflectance in the visible range decreases dramatically, which confirms the presence of TiO_2 in the composite material [55].

The band gap of the synthesized TZF photocatalysts (Table 1) with four different compositions of TiO_2 were found to be lower than the P-ZF photocatalyst. In comparison to the P-ZF catalyst, the band edge value of the synthesized 10-TZF nanocomposite gets increased towards visible region up to ≈11 nm (Fig. 3(b)). This may be due to two reasons: the mixing effect of bandgap on the composite and the interfacial coupling effect between ZF and TiO_2 [56]. For comparison, UV-vis DRS for the mechanically crushed P-ZF with 20 wt% P25 (20-MTZF) was also done, which shows the increase in band gap value (Table 1). This suggests that for the case of 20-MTZF, TiO_2 was not inserted in the pores of ZF like the TZF catalysts synthesized by solution combustion method. The red shift observed in the UV-vis DRS of our synthesized TZF catalysts is similar to the reported work with the same type of TZF nanocomposite catalysts (with different TiO_2 loadings) synthesized by citrate gel auto combustion method [57]. The changes in band gap and the band edge values of their synthesized TZF catalysts were also associated with the interaction of two semiconductors at the interface, which is comparable to our work.

3. Surface Area Analysis

The specific surface area, pore diameter and pore volume were investigated for the synthesized P-ZF and TZF photocatalysts. The results (Fig. 4(a)) show the typical type III isotherm with H_3 hysteresis loop for the synthesized P-ZF and 20-MTZF photocatalyst possesses mesoporosity, which denotes the weak adsorbent-adsorbate interactions. The H_3 hysteresis loop denotes the formation of non-uniform sized pores from the aggregated or agglomerated particles. Fig. 4(a) shows that the type IV isotherm with H_1 hysteresis

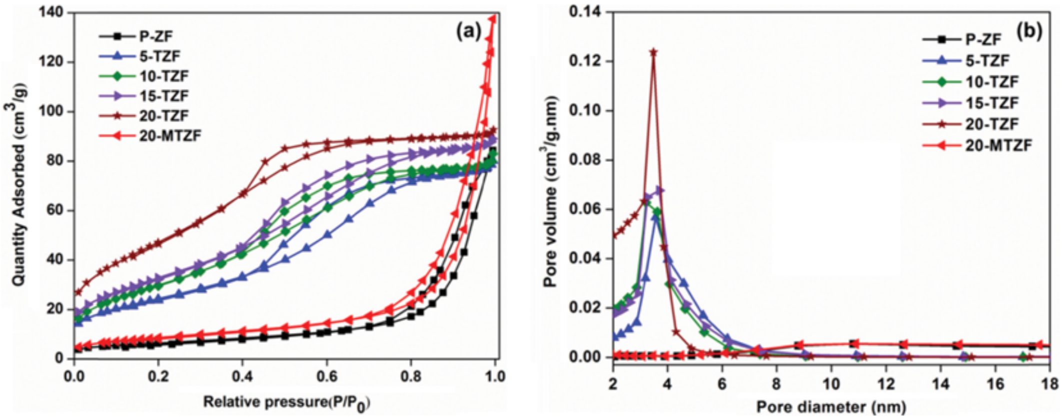

Fig. 4. N_2 adsorption and desorption isotherm (a). Pore size distribution plot of the synthesized P-ZF, TZF and 20-MTZF photocatalysts (b).

loop was obtained for the case of other TZF composite photocatalysts, which also confirms the mesoporosity of the materials. And, the H_1 hysteresis loop for same TZF composites denotes its characteristics for pores with non-uniform size formed from agglomerated particles [58-60].

Thus, the TZF photocatalyst with uniform sized pores gives higher photocatalytic activity rather than the P-ZF and 20-MTZF. Fig. 4(b) shows the pore size distribution curves, which confirms the synthesized TZF photocatalyst displays the monomodal distribution except for the P-ZF and 20-MTZF catalyst. This demonstrates that the synthesized TZF photocatalyst is in the mesoporous range. From Fig. 4(a) and (b), it is clear that the addition of TiO_2 during the synthesis of ZF can attribute a composite having type IV isotherm and higher surface area. The surface area (S_{BET}), pore diameter (D_{pore}) and pore volume (V_{total}) of the synthesized P-ZF, TZF and 20-MTZF photocatalyst (Table 1) shows the increasing trend in surface area with the decrease in pore diameter. The increase in surface area as well as the reduction in particle size can lead to more active surface areas for the enhanced photocatalytic activity. Also, the higher surface area of the synthesized TZF photocatalyst can assist the adsorption of dye molecules over its surface. This leads to the more contact of free radicals with dye molecules, thus giving more degradation efficiency [61]. Table 1 shows that the pore diameter of P-ZF catalyst was found to be 16.4 nm, and there is a sharp inflection of the adsorption branch at the relative pressure of 0.8, which denotes the capillary condensation within uniform pores. Whereas, the average pore diameter for the T-ZF catalysts decreased to 3.9 nm, and the adsorption branch shows sharp inflection at the relative pressure around 0.4. This characteristic difference from the P-ZF catalysts is attributed to the pore filling by TiO_2 inside the ZF catalyst. The increase in surface area and the decrease in pore size with the increase in TiO_2 percentages for the case of our synthesized TZF catalysts were analogous to the reported works [43,64]. This indicates that the presence of TiO_2 in host ZF matrix affects the surface area as well as the pore size, which eventually enhances its photocatalytic efficiency for RhB dye degradation.

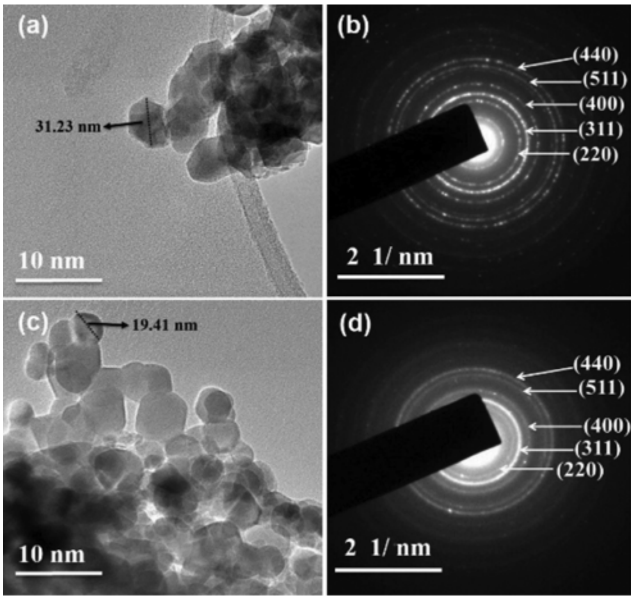

Fig. 5. TEM images of P-ZF and 10-TZF (a) & (c). SAED pattern of P-ZF and 10-TZF (b) & (d).

4. Transmission Electron Microscopy Analysis

TEM image and SAED pattern of the synthesized P-ZF and 10-TZF photocatalyst are depicted in Fig. 5. It can be observed that the synthesized P-ZF nanoparticles were spinal in shape as shown in Fig. 5(a), and Fig. 5(b) shows the SAED pattern, a typical one for the ZF structure, which depicts the nanocrystallinity of the material.

This is similar to the reported work by Deliyanni et al. [62]. The image of 10-TZF (Fig. 5(c)) seems the same as like the structure of P-ZF catalyst (Fig. 5(a)). The tightly coupled TiO_2 over the surface of ZF matrix which ultimately supports the effective charge transfer between TiO_2 and $ZnFe_2O_4$. Thus, the separation of photogenerated electron-hole pairs gets enhanced, consequently enhancing its photocatalytic performance. The morphological characterization in this study was comparable to the reported work which also depicts the close package of TiO_2 and ferrite nanoparticles [63]. Fig. 5(d) shows the SAED pattern of the 10-TZF catalyst retained as like obtained for the P-ZF catalyst, which confirms that there is no change in the crystal structure even after the formation of composite.

In addition, the presence of TiO_2 in the case of 10-TZF catalyst was confirmed by the EDS spectra (Fig. 6). The result shows the peaks which are attributed to Titanium, Zinc, Iron, Oxygen, and the peak at 8 eV corresponds to Copper grid. Moreover, the particle size of the synthesized P-ZF and 10-TZF catalysts has also been determined to be ≈31.23 and ≈19.41 nm (Fig. 5(a) and (c)). These values can be comparable with the crystallite size of the same catalysts calculated using Scherrer's formulae (Eq. (1)).

5. Photocatalytic Degradation of RhB Dye

By considering the band edge of the synthesized photocatalysts, primarily the photocatalytic activity of the synthesized P-ZF and TZF photocatalysts was evaluated for the photocatalytic degradation of RhB dye aqueous solution under RLED irradiation. Fig. 7(a) shows that 10-TZF photocatalyst gives nearly 100% degradation rate under RLED irradiation at the end of 3 h. Whereas, 80.4, 91, 83.7 and 63.03% degradation was achieved for the case of P-ZF, 5-TZF, 15-TZF, and 20-TZF photocatalysts at the end of 4 h, respectively. However, the degradation of RhB dye was found only 2% in absence of any catalysts under RLED irradiation. The enhanced degradation rate is mainly attributed to the presence of TiO_2 which effectively suppresses the electron hole recombination. And also the

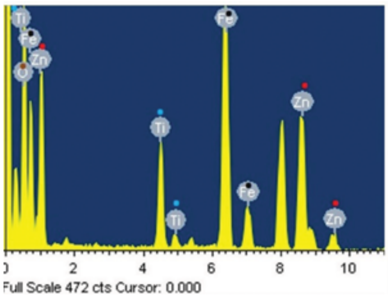

Element	Weight%
O	35.90
Ti	11.60
Fe	35.24
Zn	17.26
Totals	100.00

Fig. 6. EDS image with percentages of Ti, O, Zn and Fe of 10-TZF catalyst.

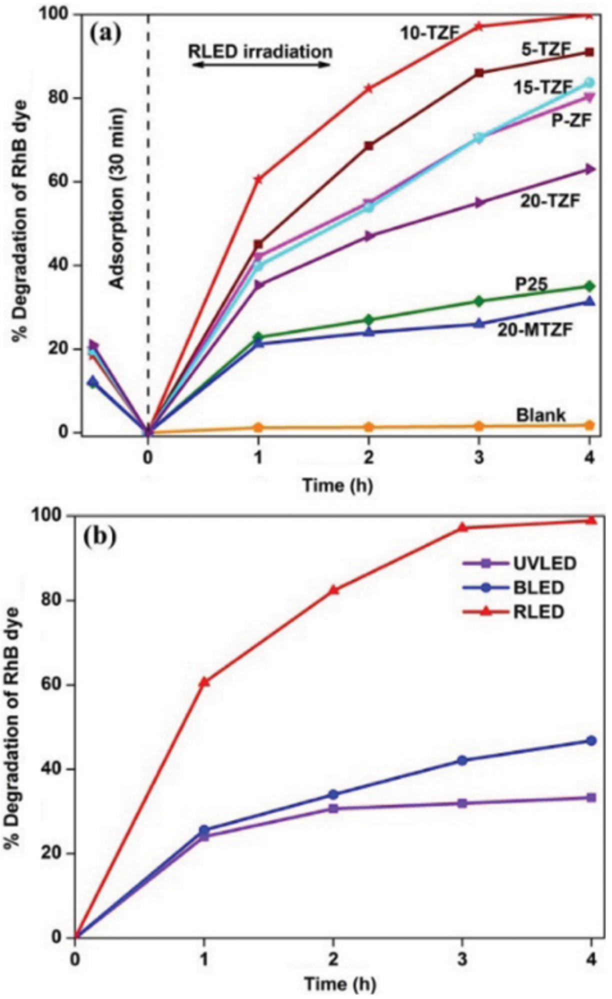

Fig. 7. Percentage degradation of RhB dye aqueous solution (1×10^{-5} M) in presence of ZF, TZF, P25 and 20-MTZF photocatalysts under RLED irradiation (a). Percentage degradation of RhB dye aqueous solution (1×10^{-5} M) in presence of 10-TZF under various LED irradiation (b).

presence of TiO_2 in the ZF composite material extended the spectral response to the visible region. Since, TiO_2 cannot be excited in the presence of visible light irradiation, the easy transformation of electrons from the conduction band of ZF to the conduction band of TiO_2 takes place, which leads to the generation of holes in the valance band of TiO_2. The photocatalytic oxidation reaction could get initiated by these holes and they may directly interact with the surface bound hydroxyl radicals [64]. It was also observed that the photocatalytic degradation decreased with the increase in TiO_2 weight percentages. This might be due to the presence of excess TiO_2 over the surface of ZF, which reduces the visible light utilization in case of 15-TZF and 20-TZF catalysts. To confirm the efficiency of the synthesized photocatalysts, the photocatalytic degradation of RhB dye aqueous solution was also carried out using P25 under RLED irradiation, and the result shows that about only 35.1% degradation (Fig. 7(a)) was attained. Additionally, the photocatalytic activity of the synthesized photocatalysts was also studied under different wavelength irradiating LED (ultraviolet and blue) under the same experimental condition. It was observed in Fig. 7(b) that the photocatalytic degradation of RhB dye under irradiation of UVLED and BLED was 33.3 and 46.8%, respectively in 4 h.

The order of degradation of RhB dye under different wavelength of LED irradiation was Red>Blue>UV. This may be due to the difference in the intensity of various LEDs utilized for the degradation reaction. It is clear that the intensity of RLED (542 lux) is much higher as compared to blue and UVLED, which may be playing a role in generation of more number of hydroxyl radicals for the degradation of RhB dye. To confirm the mineralization of the RhB dye, the chemical oxygen demand analysis was carried out, and it is found that 96% COD reduction took place after 3 h irradiation of RLED using 10-TZF catalyst. The percentage reduction of TOC value was determined to be 85% in the case of 10-TZF catalyst utilized for RhB dye degradation under RLED irradiation. The incomplete removal of TOC suggests that the photocatalytic degradation of RhB dye leads to the formation of simple organic (lower molecular weight) compounds under RLED irradiation.

It was observed (Fig. 7(b)) that there is a significant difference in the photocatalytic activity of 10-TZF catalyst with respect to UVLED, BLED and RLED irradiation. In the case of UVLED, the intensity of its light was found to be 21 lux for RhB dye degradation reactions carried out using 10-TZF catalyst. Next, in the case of BLED and RLED, the intensity of its light was determined to be 64 lux and 542 lux, respectively. The percentage degradation rises with respect to the ascending intensity: UVLED<BLED<RLED. During RLED irradiation, TiO_2 particles in 10-TZF can be effectively excited, promoting photogenerated electrons from VB ($ZnFe_2O_4$) to the CB ($ZnFe_2O_4$). Followed by this, there could be an easy migration of photo-induced electrons from the CB ($ZnFe_2O_4$) into the CB (TiO_2), leaving holes behind in the VB ($ZnFe_2O_4$) [65]. Thus, the separation of electron hole pairs takes place effectively in the case of 10-TZF under visible light (RLED) irradiation, which owns high intensity rather than in the case of UVLED and BLED. Eventually, this leads to the complete degradation of RhB dye within 3 h under RLED irradiation. Wang et al. [41] reported 100% degradation (4 h) of RhB dye using N-doped TiO_2/ZF catalyst under Xe lamp irradiation. In comparison to that study, the photocatalytic activity achieved in this study is much better than the profound studies in concern with RhB dye degradation. In particular, the utilization of ZF and TZF catalysts was so far applied for the studies of RhB dye degradation under conventional lamp sources which consume more energy [42,44]. As the LEDs were considered to be an energy efficient source for photocatalysis which could be a suitable alternative for xenon, mercury vapour and halogen lamp sources, our study utilizing visible (RLED) light is found to be an effective approach for photocatalytic applications.

6. Analysis of Hydroxyl Radicals

The photocatalytic degradation of organic dyes is always accompanied due to the presence of hydroxyl radicals. The analysis of hydroxyl radical generation was studied for 10-TZF nanocomposite using TPA as a probe molecule. Fig. 8(a) shows the fluorescence spectra of 2-hydroxy terephthalic acid in which the intensity of the peak centered at 425 nm increases up to 4 h under RLED irradiation.

Usually, the intensity of fluorescence spectra is directly propor-

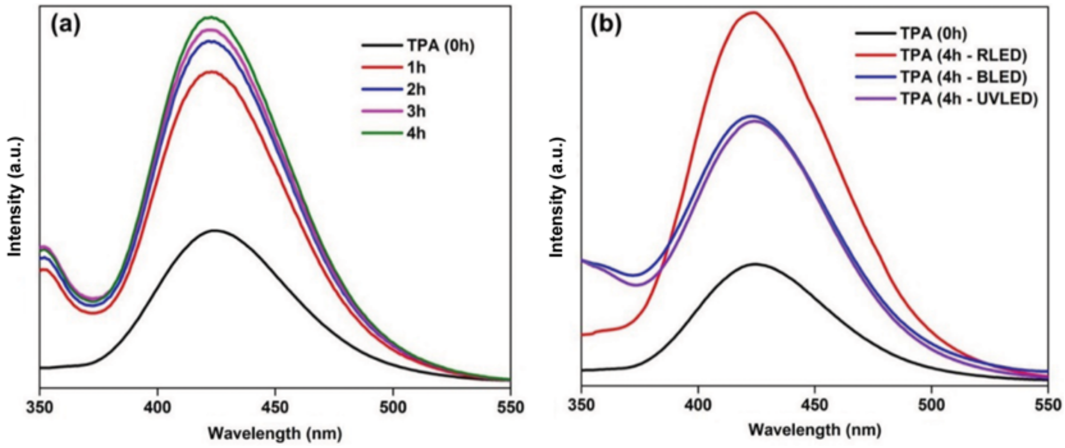

Fig. 8. Photoluminescence spectra of TPA in presence of 10-TZF under RLED irradiation up to 4 h (a). Photoluminescence spectra of TPA in presence of 10-TZF under UVLED, BLED and RLED irradiation at the end of 4 h (b).

tional to the formation of hydroxyl radicals. In Fig. 8(a) there is a gradual increase in the intensity of the peak, which implies the formation of hydroxyl radicals. This suggests that the hydroxyl radicals are the main active species for the photocatalytic process of RhB/TZF system and this is in agreement with the reported literature [66]. A hydroxyl radical analysis has also been carried out under UVLED and BLED irradiation for the same experimental conditions. Fig. 8(b) shows that the intensity of 2-hydroxy terephthalic acid was lesser than the one obtained under RLED irradiation. This confirms that the formation of more hydroxyl radicals favors 100% degradation rate of RhB dye aqueous solution in presence of 10-TZF at the end of 4 h in the case of RLED rather than the UVLED and BLED irradiation.

7. Kinetic Analysis of Degradation

The most important factor to determine the reaction mechanism for heterogeneous photocatalytic degradation reaction is kinetic analysis. A kinetic analysis was done for the photocatalytic degradation of RhB dye aqueous solution carried out under UVLED, BLED and RLED irradiation [concentration of RhB dye=1×10^{-5} M, pH=6.5, catalyst amount=25 mg (10-TZF)]. The results showed that the photocatalytic degradation reaction follows pseudo first-order kinetics (Eq. (2)),

$$\ln C_0/C_t=k_{app}t \qquad (2)$$

where C_0 is the initial concentration of dyes and C_t is the concentration at time t. The apparent first-order rate constant k_{app} was calculated by the linear regression of the slope of ln C_0/C_t vs time plot, which is depicted in Fig. 9. The initial rate was calculated for the degradation of RhB dye aqueous solution under UVLED, BLED and RLED, which was found to be 0.4, 0.6 and 3.6×10^{-7} molL^{-1}. Whereas, the regression coefficient (R^2) was calculated to be 0.85, 0.93 and 0.99. Fig. 9 shows that the experiments carried out for the degradation of RhB dye aqueous solution follows pseudo first-order kinetics. The regression coefficient (R^2=0.99) for the case of RLED, suggests that the degradation of RhB dye fits the Langmuir Hinshelwood kinetic model.

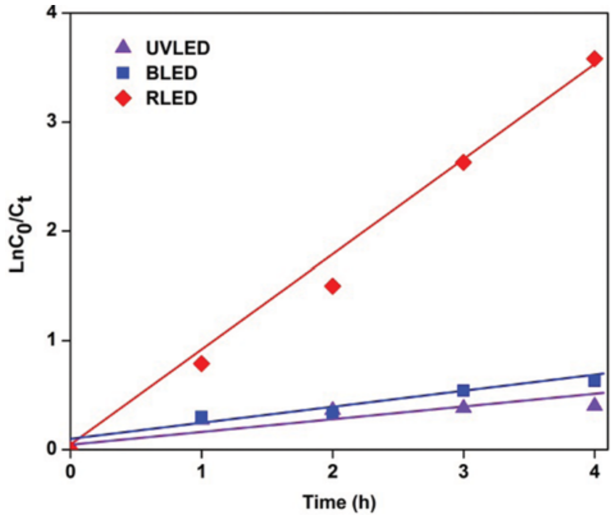

Fig. 9. Kinetic study for the degradation of RhB dye aqueous solution (1×10^{-5} M) for the case of 10-TZF under UVLED, BLED and RLED irradiation.

The initial rate value of RhB dye degradation in presence of RLED irradiation using 10-TZF photocatalyst was six- and nine-times higher than BLED and UVLED, respectively. This confirms that RLED is the effective light source for the photocatalytic degradation of RhB dye aqueous solution using 10-TZF photocatalyst. As explained previously (section 5), the photocatalytic activity of the synthesized 10-TZF catalyst varies with the type of LED irradiation. The kinetics in concern with the RLED utilized reaction outputs maximum efficiency rather than in the case of UVLED and BLED. This indicates that the divergence in the intensities about the different LEDs (discussed in section 5) makes a major difference in concern with RhB dye degradation.

8. Effect of Operational Parameters

It is well known that various operational parameters play a major role in the photocatalytic degradation of various organic compounds present in water. In this study, we tried to study the effect of RhB dye concentration, pH and catalyst amount using10-TZF photocatalyst.

8-1. Effect of Catalyst Amount

To find the optimum amount of catalyst loading in the case of

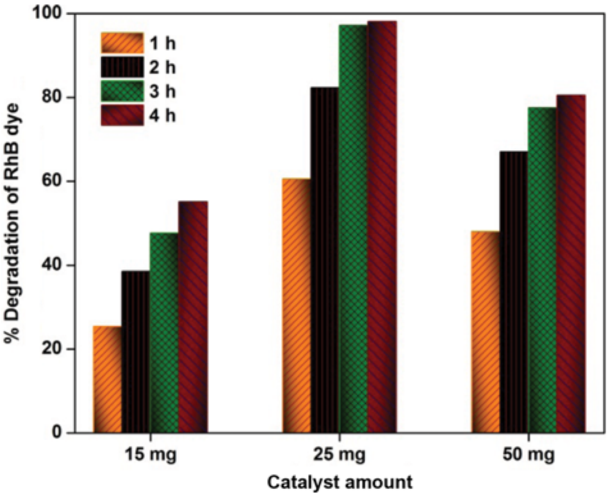

Fig. 10. Effect of catalyst amount for the degradation of RhB dye (1×10^{-5} M) using 10-TZF photocatalyst under RLED irradiation.

10-TZF for the photocatalytic degradation of RhB dye aqueous solution, the amount of catalyst was varied by keeping the concentration and amount of the dye solution constant (1×10^{-5} M; 25 ml) for all the experiments. Fig. 10 shows that the percentage degradation was 55.1, 98.09 and 80.5% achieved for 15, 25 and 50 mg amount of 10-TZF catalyst, respectively, at the end of 4 h. It was observed that 25 mg 10-TZF catalyst loading was the optimum one for the degradation of RhB dye aqueous solution. The percentage degradation reached a maximum in the case of 25 mg catalyst amount, whereas it was reduced to 80.5% at 50 mg catalyst amount. This demonstrates that the higher loading (50 mg) of suspended catalyst increase the turbidity leads to the lesser light penetration or light scattering and screening effect, which ultimately leads to the lower degradation rate [67].

8-2. Effect of pH

The pH of the solution is one of the most important parameters affecting the degradation of RhB dye on the surface of photocatalyst. The effect of pH over the photocatalytic degradation of RhB dye was studied using 10-TZF catalyst, by varying the pH from 2-12 of the RhB dye aqueous solution using HCl and NaOH solution under irradiation of RLED. Fig. 11 reveals that the lowest degradation was attributed to pH=2 and it was increased with increase in pH value up to pH=10. The decrease in percentage degradation at lower pH is due to the negatively charged RhB dye species under experimental conditions and its higher adsorption rate and also at acidic conditions the slower degradation rate was ascribed to the scavenging of hydroxyl radicals by H^+ ions [68,69]. However, with the increase in pH from 10 to 12 it was found that there is slight decrease in the photocatalytic degradation, and this may be due to the agglomerate formation of hydroxides which reduces the transmission of irradiation [70,71].

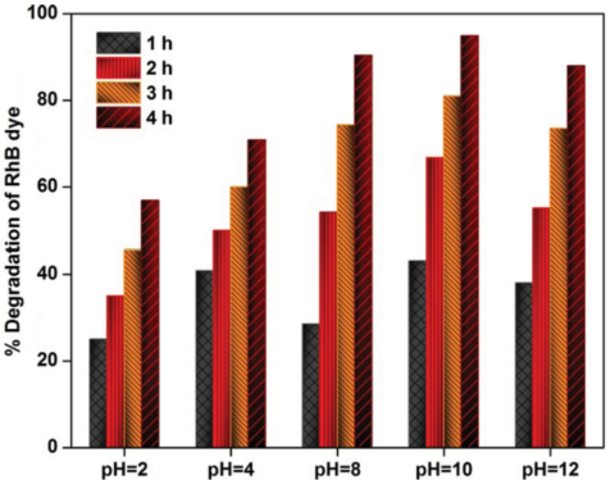

Fig. 11. Effect of pH for the degradation of RhB dye (1×10^{-5} M) using 10-TZF (25 mg) photocatalyst under RLED irradiation.

8-3. Effect of RhB Dye Concentration

To study the effect of RhB dye degradation under RLED irradiation, the concentration of the dye was varied from 1×10^{-5} M to 4.18×10^{-5} M by keeping the amount of catalyst as 25 mg in all the experiments. It is observed in Fig. 12 that the percentage degradation of 1, 2.1, 3.08 and 4.18×10^{-5} M concentration of RhB dye was 98%, 88%, 74.05% and 51.47%, respectively, in 4 h under irradiation of RLED.

These results, which are similar to the previous reported work on the degradation of RhB dye using various photocatalysts, clearly indicate that the increase in concentration of dye reduces the degradation. This is ultimately due to the greater amount of dye adsorption over the catalyst surface with increase in concentration of the dye solution [72]. And also, fewer photons reach over the surface of the catalyst at higher dye concentration. Eventually, there is an ultimate reduction in the number of ·OH and O_2·- radicals, which leads to the decrease in photocatalytic activity.

9. Recyclability

The recyclability of the synthesized 10-TZF catalyst was evaluated for the degradation of RhB dye aqueous solution up to five

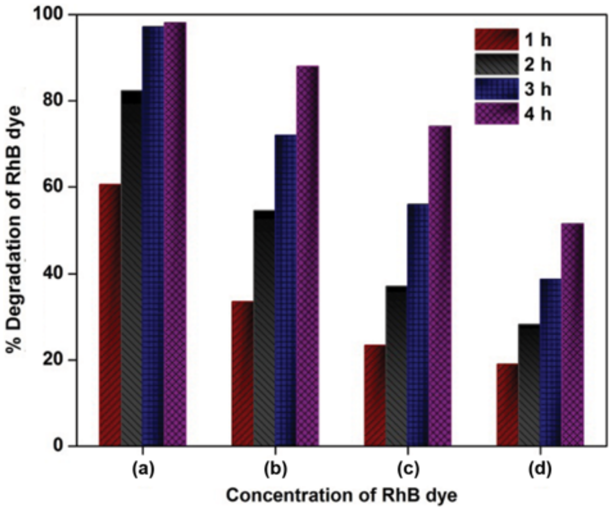

Fig. 12. Effect of dye concentration for the degradation of RhB dye using 10-TZF photocatalyst (25 mg) under RLED irradiation [1×10^{-5} M (a), (b) 2.1×10^{-5} M, (c) 3.08×10^{-5} M and (d) 4.18×10^{-5} M].

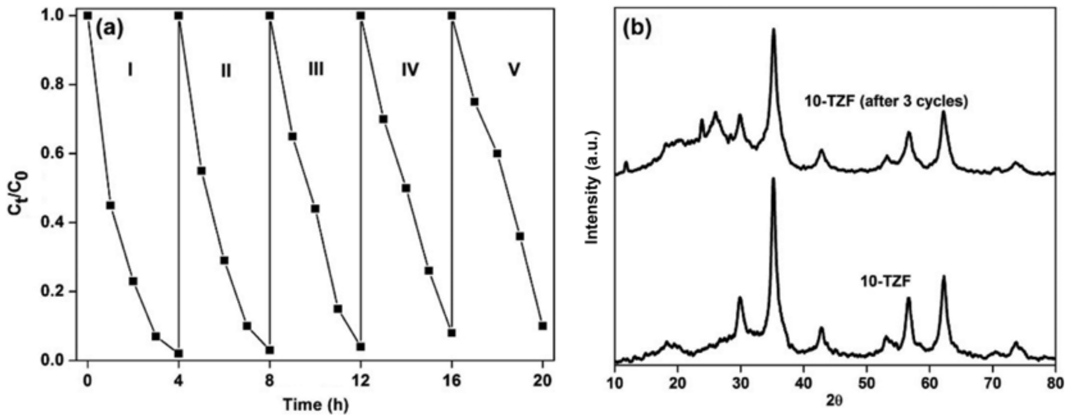

Fig. 13. Recyclability (a) XRD patterns of 10-TZF catalyst under RLED irradiation for RhB dye degradation (b).

cycles under RLED irradiation. Fig. 13(a) shows the photocatalytic activity of the 10-TZF catalyst was reduced up to 2-4% at the end of 4 h for each reaction. The XRD pattern in Fig. 13(b) also reveals that there is no change in the crystal structure of the 10-TZF catalyst before and after five cycles of the reaction. This also depicts that 10-TZF could be an effective recyclable catalyst for the degradation of RhB dye aqueous solution under RLED irradiation.

10. Mechanism of Photocatalytic Degradation Using 10-TZF Catalyst on Pollutant

Under RLED irradiation, the photocatalytic degradation of RhB was effectively achieved using 10-TZF catalyst. This could be possible only because of the formation of superoxide anion ($^{\bullet}O_2^-$) and hydroxyl radicals ($^{\bullet}OH$), which leads to effective degradation. The formation of these type of radicals is always favored by the conduction and valance band edge position of TiO_2 and ZF in 10-TZF catalyst. This can be explained by the simple representation (Fig. 14) for the 10-TZF catalyst responsible for visible light (RLED) activity. The electron transfer from ZF to TiO_2 or the hole transfer from TiO_2 to ZF is feasible in 10-TZF catalyst during photocatalytic reactions. As the conduction band potential of TiO_2 (E_{CB}=−0.30 eV) is less than that for ZF (E_{CB}=−1.54 eV [73]) paves way for the electron transfer from ZF to TiO_2.

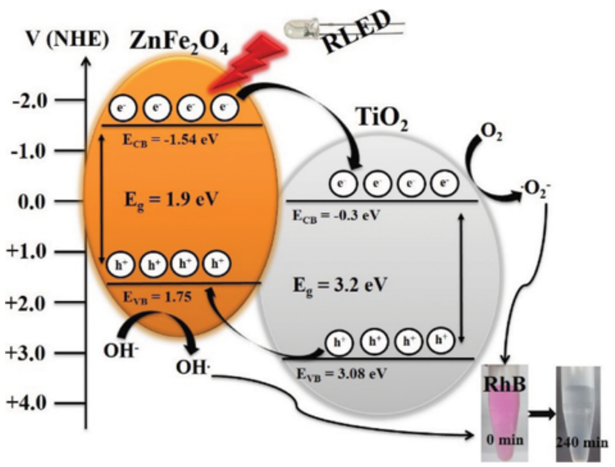

Fig. 14. Plausible electron transfer process in 10-TZF for the degradation of RhB dye under RLED irradiation.

Besides, the valance band potential of ZF (E_{VB}=0.38 eV [74]) is higher than for TiO_2 (E_{VB}=0.38 eV), which makes the holes transfer from TiO_2 to ZF. Ultimately, there could be a reduction in the recombination of electron-hole pairs at this stage. The photogenerated electrons and holes generated by ZF and TiO_2 can react with the surface adsorbed O_2 and H_2O to form $^{\bullet}O_2^-$ and $^{\bullet}OH$. These radicals have strong oxidation potential, which can oxidize RhB dye present over the active sites of the composites eventually into lower molecular weight compounds namely CO_2 and H_2O [43]. Thus, it can be concluded that the formation of $^{\bullet}O_2^-$ and $^{\bullet}OH$ radicals is attributed to the conduction and valance band edge positions of 10-TZF catalyst upon visible light (RLED) irradiation.

11. Proposed Mechanism for the Degradation of RhB Dye

For any photocatalytic degradation reaction, the identification of believable intermediates is the finest way to understand the deg-

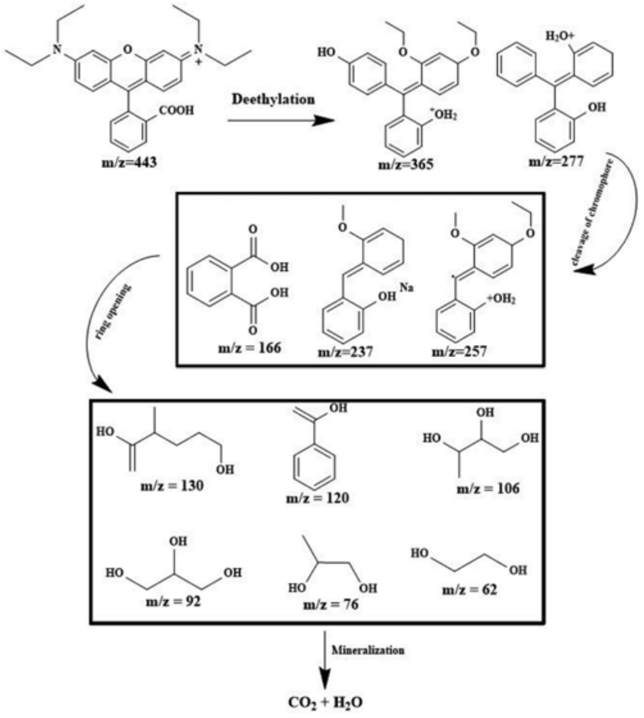

Fig. 15. Plausible degradation pathway for RhB dye degradation.

radation mechanism. In this study, ESI-MS experiments were conducted to identify the intermediates for the degraded RhB dye aqueous solution in presence of 10-TZF under RLED irradiation (Fig. S1-S5 of ESI†). It was observed in Fig. 15 that the RhB dye chromophore was degraded completely via four processes: (i) Deethylation, (ii) cleavage of chromophores, (iii) ring openings, and (iv) mineralization. In our study, the degradation pathway is slightly different from the reported literature in concern with the degradation of RhB dye aqueous solution [75]. Initially, deethylation leads to the formation of phenyl oxonium intermediate with the m/z of 365 and 277 as major products (Fig. S2 of ESI†). Then the cleavage of chromophore leads to the formation of major phenolic intermediates with the m/z 257 and 237. The formation of primary oxidation product remarkably phthalic acid with m/z of 166 (Fig. S3 and S4 of ESI†) originated due to the chromophore cleavage. These compounds were further degraded to lower molecular weight alcoholic compounds: 4-methylhex-5-ene-1,5-diol (m/z=130), 1-phenylethen-1-ol (m/z=120), butane-1,2,3-triol (m/z=106), propane-1,2,3-triol (m/z=92), propane-1,2-diol (m/z=76) and ethane-1,2-diol (m/z =62).

Finally, these alcoholic compounds were mineralized to CO_2 and H_2O. It is clear that the whole fragmentation of intermediates is ascribed to the $^{\bullet}OH$ or photogenerated hole which could directly attack the central carbon of RhB dye molecule [76,77].

12. Comparison for Degradation of RhB Dye

The photocatalytic efficiency of synthesized P-ZF and TZF with RLED was compared with the reported work. There is no report so far for the degradation of RhB dye aqueous solution utilizing titania ferrite nanocomposites under energy efficient RLEDs. Table 1 of ESI† shows the comparison data of our study with some of the reported work which has been done utilizing UV and Xe lamp as an irradiation source. In comparison to the reported work, our study outperforms for the degradation of RhB dye aqueous solution under RLEDs within 3 h. Moreover, RLED consumes low power rather than needed for the conventional lamp sources for the photocatalytic reaction. Thus, RLEDs could be a good alternative for the photocatalytic degradation of various organic compounds.

CONCLUSIONS

P-ZF and TZF have been synthesized by sol-gel auto combustion method and successfully applied for the degradation of aqueous RhB dye solution under ultraviolet and visible LEDs. The bandgap of the TZF composites was found in the range of 1.95 to 2.05 eV. The surface area of the TZF photocatalyst increased with the increase in the amount of TiO_2. The XRD patterns of the zinc ferrite were unaltered; however, slight broadening in the peak corresponds to 2θ at 35.5° due to incorporation of TiO_2 in the zinc ferrite pores. Among all the synthesized catalysts, zinc ferrite containing 10 wt% TiO_2 (10-TZF) displayed the highest photocatalytic activity under irradiation of RLED. It was found that an increase in hydroxyl radical generation leads to the higher photocatalytic activity. The hydroxyl radical generation was found to be highest in presence of RLED irradiation using 10-TZF under experimental conditions, which demonstrated higher photocatalytic activity. The efficiency of the synthesized 10-TZF photocatalyst was verified using UVLED and BLED under the same experimental conditions. Also, the initial rate of degradation under RLED was six- and nine-times higher than that of BLED and UVLED, respectively. Additionally, the degradation pathway of RhB dye was studied for the degradation reaction carried out under RLED. It is concluded that the TiO_2 incorporated zinc ferrite having 10 wt% TiO_2 can attribute highest photocatalytic activity under the irradiation of RLED and with increasing number of LED may be useful for degradation of RhB dye having higher concentration.

ACKNOWLEDGEMENTS

This work was supported by the Department of Science and Technology (DST) - New Delhi, India funding for a project under "Fast Track Proposals for Young Scientists Scheme - (SR/FT/CS - 027/2009)". Authors acknowledge CSMCRI for allowing publication of this work (Grant number: CSIR-CSMCRI - 051/2015). Kalithasan Natarajan is thankful to AcSIR-CSMCRI for enrolment in PhD programme. We are also thankful to Mr. Pradip Parmar, Mr. Mahesh Sanghani, Mr. Gopal and Analytical Science Discipline of the institute for kind support.

SUPPORTING INFORMATION

Additional information as noted in the text. This information is available via the Internet at http://www.springer.com/chemistry/journal/11814.

REFERENCES

1. M. R. Hoffman, S. T. Martin, W. Choi and D. W. Bahnemann, *Chem. Rev.*, **95**, 69 (1995).
2. Y. Xu and C. H. Langford, *Langmuir.*, **17**, 897 (2013).
3. X. Chen and S. S. Mao, *Chem. Rev.*, **107**, 2891 (2007).
4. Y. Ma, X. Wang, Y. Jia, X. Chen, H. Han and C. Li, *Chem. Rev.*, **114**, 9987 (2014).
5. R. Thiruvenkatachari, S. Vigneswaran and S. Moon, *Korean J. Chem. Eng.*, **25**, 64 (2008).
6. R. J. Tayade, R. G. Kulkarni and R. V. Jasra, *Ind. Eng. Chem. Res.*, **45**, 922 (2006).
7. M. Saquib and M. Muneer, *Dyes Pigm.*, **53**, 237 (2002).
8. J. Theurich, M. Lindner and D. W. Bahnemann, *Langmuir.*, **12,** 6368 (1996).
9. M. A. Wurtele, T. Kolbe and M. Lipsz, *Water Res.*, **45**, 1481 (2011).
10. I. A. Soloshenko, V. Y. Bazhenov and V. A. Khomich, *IEEE Trans Plasma Sci.*, **34**, 1365 (2006).
11. W. Y. Wang and I. Ku, *Water Res.*, **40**, 2249 (2006).
12. F. Akbal, *Environ. Prog.*, **24**, 317 (2005).
13. R. J. Tayade, T. S. Natarajan and H. C. Bajaj, *Ind. Eng. Chem. Res.*, **48**, 10262 (2009).
14. M. Hajaghazadeh, V. Vaiano and D. Sannino, *Korean J. Chem. Eng.*, **32,** 636 (2015).
15. S. Dominguez, P. Ribao and M. J. Rivero, *Appl. Catal. B: Environ.*, **178**, 165 (2015).
16. M. Marchelek, B. Bajorowicz and P. Mazierski, *Catal. Today*, **252**, 47 (2015).

17. M. R. Rasoulifard, M. Fazli and M. R. Eskandarian, *J. Ind. Eng. Chem.*, **24**, 121 (2015).
18. W. K. Jo and R. J. Tayade, *Chinese J. Catal.*, **35**, 1781 (2014).
19. S. Yin, B. Liu, P. Zhang, T. Morikawa, K. Yamanaka and T. Sato, *J. Phys. Chem. C.*, **112**, 12425 (2008).
20. K. Dai, J. Lv and L. Lu, *Mater. Lett.*, **130**, 5 (2014).
21. K. V. SubbaRao, B. Lavedrine and P. Boule, *J. Photochem. Photobiol. A.*, **154**, 189 (2003).
22. S. Bingham and W. A. Daoud, *J. Mater. Chem.*, **21**, 2041 (2011).
23. L. Jing, W. Zhou and G. Tian, *Chem. Soc. Rev.*, **42**, 9509 (2013).
24. J. H. Pan, H. Dou and Z. Xiong, *J. Mater. Chem.*, **20,** 4512 (2010).
25. S. Yan, W. Ling and E. Zhou, *J. Cryst. Growth.*, **273**, 226 (2004).
26. Y. Bai, J. Zhou, Z. Gui and L. Li, *Mater. Chem. Phys.*, **98**, 66 (2006).
27. J. S. Jang, S. J. Hong and J. S. Lee, *J. Korean Phys. Soc.*, **54**, 204 (2009).
28. S. Sun, X. Yang, Y. Zhang, F. Zhang, J. Ding, J. Baoa and C. Gao, *Prog. Nat. Sci.*, **22**, 639 (2012).
29. K. J. McDonald and K. S. Choi, *Chem. Mater.*, **23**, 4863 (2011).
30. S. Xu, D. Feng and W. Shangguan, *J. Phys. Chem. C.*, **113**, 2463 (2009).
31. S. S. Srinivasan, J. Wade and E. K. Stefanakos, *J. Nanomater.*, **45712**, 1 (2006).
32. Z. H. Yuan and L. Zhang, *J. Mater. Chem.*, **11**, 1265 (2001).
33. R. S. Puche, M. J. T. Fernandez, V. B. Gutierrez, R. Gomez, V. Marquina, M. L. Marquina, J. L. P. Mazariego and R. Ridaura, *Bol. Soc. Esp. Ceram. V.*, **47**, 133 (2008).
34. E. M. M. Ewais, M. M. Hessien and A. A. El-Geassy, *J. Aust. Ceram. Soc.*, **44**, 57 (2008).
35. R. Dom, R. Subasri, K. Radha and P. H. Borse, *Solid State Commun.*, **151**, 470 (2011).
36. P. Sivakumar, R. Ramesh, A. Ramanand, S. Ponnusamy and C. J. Muthamizhchelvan, *Mater. Lett.*, **66**, 314 (2012).
37. H. Kaur, J. Singh and B. S. Randhawa, *Ceram. Int.*, **40**, 12235 (2014).
38. Z. Zhang and W. Wang, *Mater. Lett.*, **133**, 212 (2014).
39. X. Cao, L. Gu, X. Lan, C. Zhao, D. Yao and W. Sheng, *Mater. Chem. Phys.,* **106**, 175 (2007).
40. M. Ge, Y. Chen, M. Liu and M. Li, *J. Environ. Chem. Eng.*, **3**, 2809 (2015).
41. Y. Yao, J. Qin, H. Chen, F. Wei, X. Liu, J. Wang and S. Wang, *J. Hazard Mater.*, **291**, 28 (2015).
42. J. Li, Q. Xiao, L. Li, J. Shen and D. Hu, *Appl. Surf. Sci.*, **331**,108 (2015).
43. Q. Xu, J. Feng, L. Li, Q. Xiao and J. Wang, *J. Alloys Compd.*, **641**, 110 (2015).
44. G. Zhang, Y. Sun, D. Gao and Y. Xu, *Mater. Res. Bull.*, **45**, 755 (2010).
45. B. Zhang, J. Zhang and F. Chen, *Res. Chem. Intermed.*, **34**, 375 (2008).
46. J. Yang, X. Li, X. Deng, Z. Huang and Y. Zhang, *J. Ceram. Soc. Jpn.*, **120**, 579 (2012).
47. X. Li, Y. Hou, Q. Zhao and L. Wang, *J. Colloid Interface Sci.*, **358**, 102 (2011).
48. C. C. Chen, E. Butler, M. A. Ahmad, Y. T. Hung and Y. P. Fu, *Mater. Res. Bull.*, **50**, 178 (2014).
49. T. Tangcharoen, A. Ruangphanit, W. Klysubun and W. Pecharapa, *J. Sol-Gel Sci. Technol.*, **66**, 387 (2013).
50. J. Azadmanjiri, *Mater. Chem. Phys.*, **109**, 109 (2008).
51. R. Zhang, J. Huang, J. Zhao, Z. Sun and Y. Wang, *Energy Fuel*, **21**, 2682 (2007).
52. A. Tang, Y. Deng, J. Jin and H. Yang, *Sci. World J.*, Article ID **480527**, 1 (2012).
53. M. Bandyopadhyay, A. Birkner, M. W. E. Berg, K. V. Klementiev, W. Schmidt, W. Grunert and H. Gies, *Chem. Mater.*, **17**, 3820 (2005).
54. P. H. Borse, J. S. Jang, J. S. Lee, F. N. Khan, M. G. Ha, J. P. Kim, J. S. Bae, E. D. Jeong and H. G. Kim, *J. Korean Phys. Soc.*, **59**, 2750 (2011).
55. H. Lv, L. Ma, P. Zeng, D. Ke and T. Peng, *J. Mater. Chem.*, **20**, 3665 (2010).
56. P. Cheng, C. Deng, M. Gu and W. Shangguan, *J. Mater. Sci.*, **42**, 9239 (2007).
57. P. P. Hankare, R. P. Patil, A. V. Jadhav, K. M. Garadkar and R. Sasikala, *Appl. Cat. B: Environ.*, **107**, 333 (2011).
58. K. S. W. Sing, *Pure Appl. Chem.*, **54**, 2201 (1982).
59. T. Xie, L. Xu and C. Liu, *RSC Adv.*, **3**, 15856 (2013).
60. A. I. Borhana, P. Samoila, V. Huleac, A. R. Iordana and M. N. Palamaru, *J. Photochem. Photobiol. A.*, **279**, 17 (2014).
61. G. Fan, Z. Gu, L. Yang and F. Li, *Chem. Eng. J.*, **155**, 534 (2009).
62. L. Nalbandian, A. Delimitis, V. T. Zaspalis, E. A. Deliyanni, D. N. Bakoyannakis and E. N. Peleka, *Micropor. Mesopor. Mater.*, **114**, 465 (2008).
63. L. Zhang, Y. He, Y. Wu and T. Wu, *Mater. Sci. Eng. B-Adv.*, **176**, 1497 (2011).
64. E. Moreira, L. A. Fraga, M. H. Mendonca and O. C. Monteiro, *J. Nanopart. Res.*, **14**, 1 (2012).
65. X. Zhu, F. Zhang, M. Wang, J. Ding, S. Suna, J. Bao and C. Gao, *Appl. Surf. Sci.*, **319**, 83 (2014).
66. X. Li, Y. Hou, Q. Zhao and L. Wang, *J. Colloid Interface Sci.*, **358**, 102 (2011).
67. A. Akyol, H. C. Yatmaz and M. Bayramoglu, *Appl. Catal. B. Environ.*, **54**, 19 (2004).
68. F. Chen, J. Zhao and H. Hidaka, *Int. J. Photoenergy,* **5**, 209 (2003).
69. S. Q. Liu, L. R. Feng, N. Xu, Z. G. Chen and X. M. Wang, *Chem. Eng. J.*, **203**, 432 (2012).
70. P. P. Hankare, A. V. Jadhav, R. P. Patil, K. M. Garadkar, I. S. Mulla and R. Sasikala, *Arch. Phys. Res.*, **3**, 269 (2012).
71. M. Nookaraju, A. Rajini, N. Venkatathri and I. A. K. Reddy, *Asian J. Chem.*, **24**, 5817 (2012).
72. X. Chen, Z. Xue, Y. Yao, W. Wang, F. Zhu and C. Hong, *Int. J. Photoenergy,* Article ID **754691** (2012).
73. C. Q. Zhu, Y. R. Li, Q. Su, B. G. Lu, J. Q. Pan, J. W. Zhang, E. Q. Xie and W. Lan, *J. Alloys Compd.*, **575**, 333 (2013).
74. J. Yin, L. J. Bie and Z. H. Yuan, *Mater. Res. Bull.*, **42**, 1402 (2007).
75. T. S. Natarajan, K. Natarajan, H. C. Bajaj and R. J. Tayade, *J. Nanopart. Res.*, **15**, 1 (2013).
76. K. Yu, S. Yang, H. He, C. Sun, C. Gu and Y. Ju, *J. Phys. Chem. A.*, **113**, 10024 (2009).
77. T. Soltani and M. H. Entezari, *Chem. Eng. J.,* **223**, 145 (2013).
78. W. Zhang, M. Wang, W. Zhao and B. Wang, *Dalton Trans.*, **42**, 15464 (2013).
79. S. Wu, X. Shen, G. Zhu, H. Zhou, Z. Ji, K. Chen and A. Yuan, *Appl. Cat. B: Environ.*, DOI:10.1016/j.apcatb.2015.11.035.

Supporting Information

Facile synthesis of $TiO_2/ZnFe_2O_4$ nanocomposite by sol-gel auto combustion method for superior visible light photocatalytic efficiency

Kalithasan Natarajan*, Puspendra Singh*, Hari Chand Bajaj*,**, and Rajesh Jagannath Tayade*,†**

*Inorganic Materials and Catalysis Division (IMCD), CSIR-Central Salt and Marine Chemicals Research Institute (CSIR-CSMCRI), Council of Scientific and Industrial Research (CSIR), G. B. Marg, Bhavnagar-364 002, Gujarat, India
**Academy of Scientific and Innovative Research (AcSIR), CSIR-Central Salt and Marine Chemicals Research Institute (CSIR-CSMCRI), G. B. Marg, Bhavnagar-364 002, Gujarat, India

(*Received 19 October 2015 • accepted 18 February 2016*)

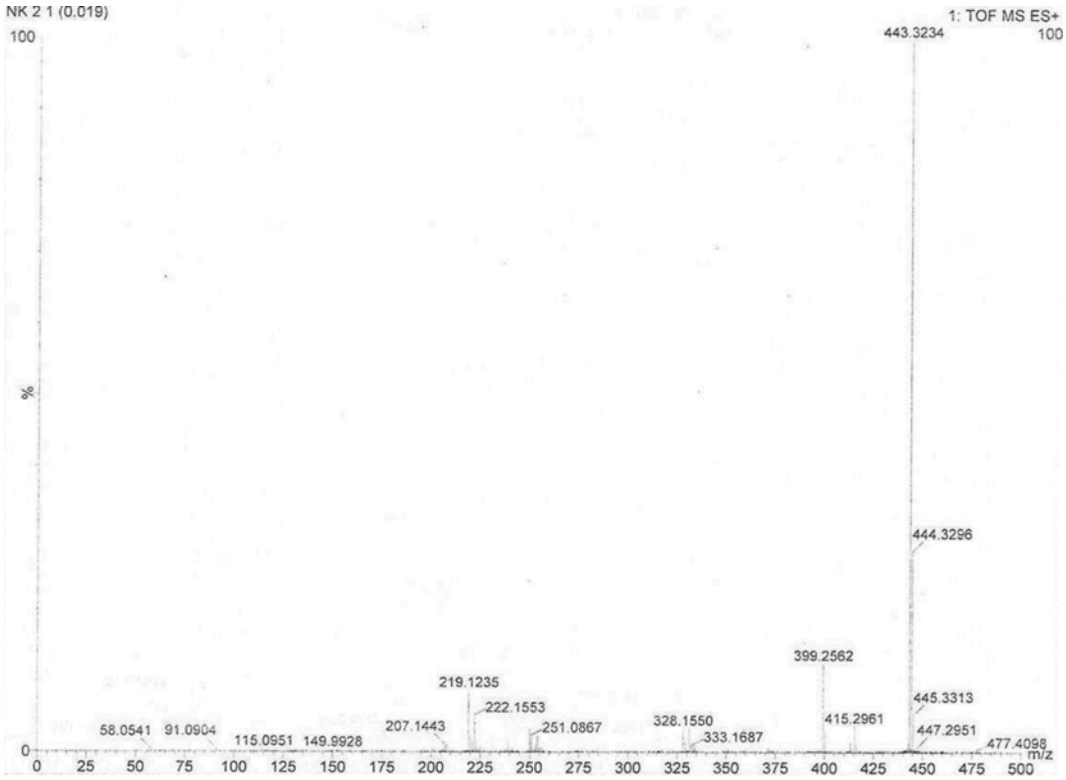

Fig. S1. ESI-MS pattern of RhB dye original solution (0 h - before reaction).

ESI-MS pattern for the photocatalytic degradation of RhB dye (1×10^{-5} M - 25 ml) in presence of 10-TZF (25 mg) under RLED irradiation.

REFERENCES

1. G. Zhang, Y. Sun, D. Gao and Y. Xu, *Mater. Res. Bull.*, **45**, 755 (2010).
2. B. Zhang, J. Zhang and F. Chen, *Res. Chem. Intermed.*, **34**, 375 (2008).
3. J. Yang, X. Li, X. Deng, Z. Huang and Y. Zhang, *J. Ceram. Soc. Jpn.*, **120**, 579 (2012).
4. X. Cao, L. Gu, X. Lan, C. Zhao, D. Yao and W. Sheng, *Mater. Chem. Phys.*, **106**, 175 (2007).
5. X. Li, Y. Hou, Q. Zhao and L. Wang, *J. Colloid Interface Sci.*, **358**, 102 (2011).
6. S. Sun, X. Yang, Y. Zhang, F. Zhang, J. Dinga, J. Bao and C. Gao, *Prog. Nat. Sci.*, **22**, 639 (2012).

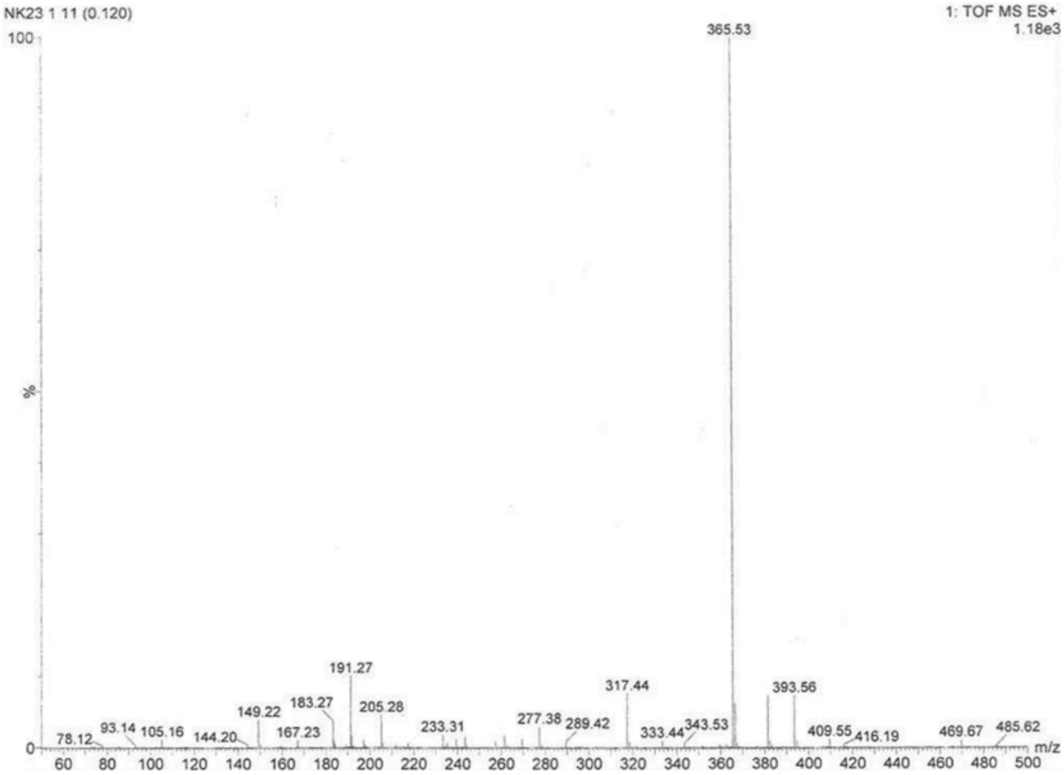

Fig. S2. ESI-MS pattern of RhB dye solution (after 1 h reaction).

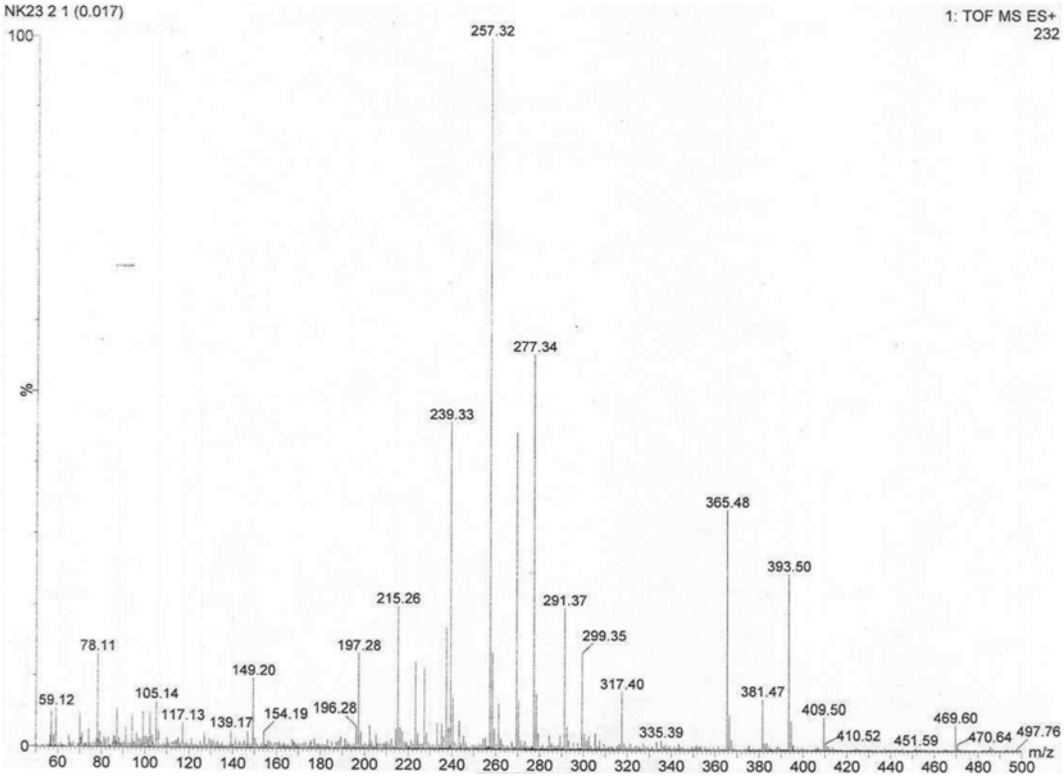

Fig. S3. ESI-MS pattern of RhB dye solution (after 2 h reaction).

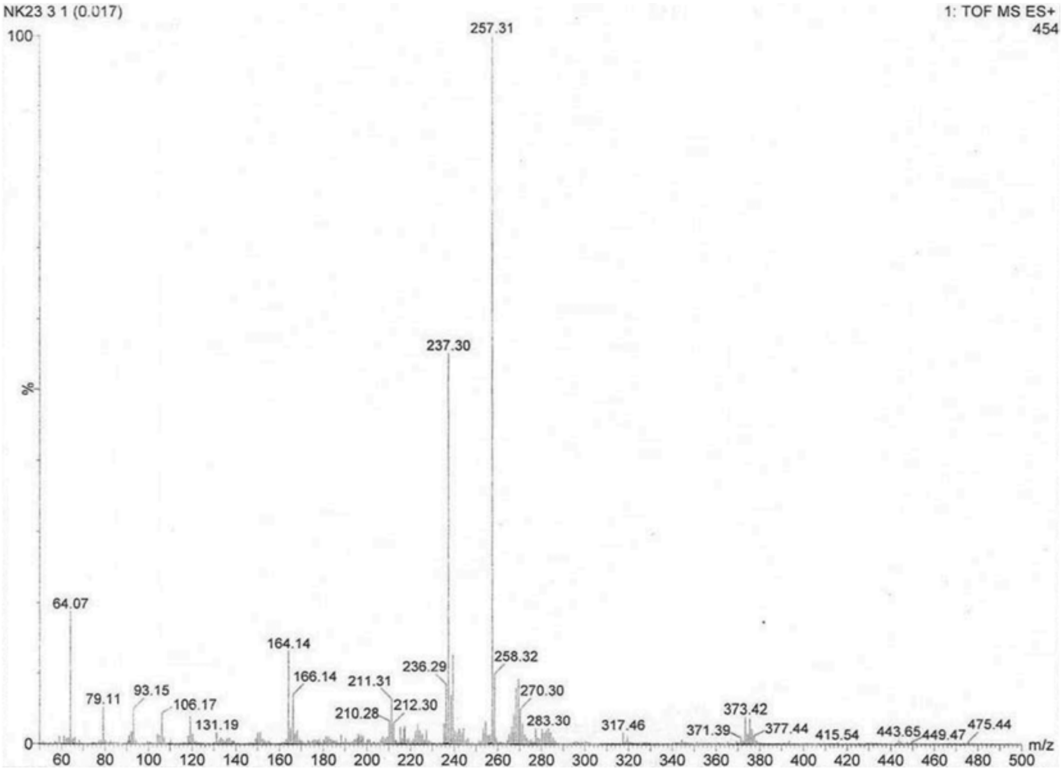

Fig. S4. ESI-MS pattern of RhB dye solution (after 3 h reaction).

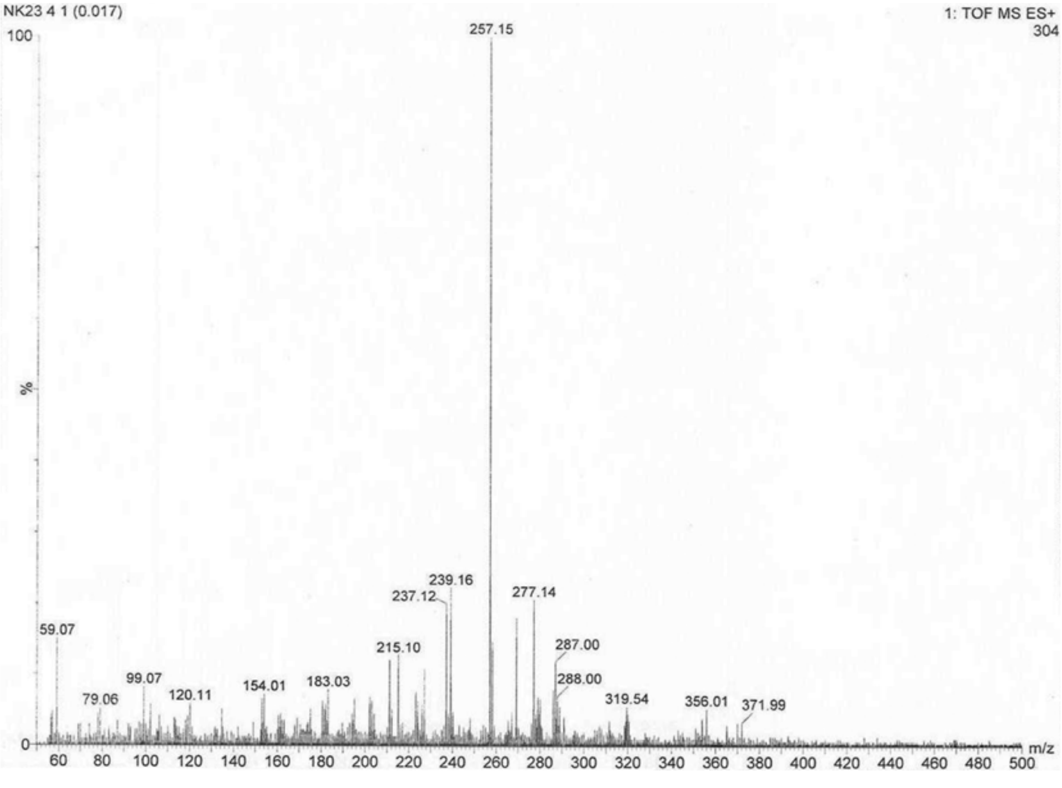

Fig. S5. ESI-MS pattern of RhB dye solution (after 4 h reaction).

Table 1. Comparison of TZF catalysts for the degradation of RhB with the reported literature

Serial no.	Catalyst	Synthesis method	Light source	Concentration of RhB dye	Time (h)	Degradation (%)	Ref.
1	$TiO_2/ZnFe_2O_4$	Hydrothermal approach	λ=254 nm (8 W)	2×10^{-5} M	2.5	99.7	1
2	$TiO_2/ZnFe_2O_4$	Sol-gel method	UV lamp (300 W)	-	3	94.4	2
3	$ZnFe_2O_4/TiO_2$ photocatalyst	Salt-assisted solution combustion method	Metal halide lamp (175 W)	2×10^{-5} M	4	97	3
4	Ag/Spinel $ZnFe_2O_4$ nanoplates	Co-precipitation method	Xe lamp (500 W)	2×10^{-5} M	2.5	100	4
5	Sphere-like zinc ferrite	One-step solvothermal method	Xe lamp (500 W)	4×10^{-5} M	5	100	5
6	Sponge like $ZnFe_2O_4$	Solution combustion method	Xe lamp (300 W)	3.9×10^{-5} M	5	90	6
7	P-ZF and TZF composites	Sol-gel auto combustion method	Red LED (5 no's, 50 mW)	1×10^{-5} M	3	10-TZF=98 (3 h) P-ZF=80 (4 h)	This study